Attenuation Correction Synthesis for Hybrid PET-MR Scanners

Ninon Burgos[1], Manuel Jorge Cardoso[1,2], Marc Modat[1,2], Stefano Pedemonte[1], John Dickson[3], Anna Barnes[3], John S. Duncan[4], David Atkinson[5], Simon R. Arridge[1], Brian F. Hutton[3,6], and Sebastien Ourselin[1,2]

[1] Centre for Medical Image Computing, University College London, London, UK
[2] Dementia Research Centre, University College London, London, UK
[3] Institute of Nuclear Medicine, University College London, London, UK
[4] Department of Clinical and Experimental Epilepsy, UCL IoN, London, UK
[5] Centre for Medical Imaging, University College London, London, UK
[6] Centre for Medical Radiation Physics, University of Wollongong, NSW, Australia

Abstract. The combination of functional and anatomical imaging technologies such as Positron Emission Tomography (PET) and Computed Tomography (CT) has shown its value in the preclinical and clinical fields. In PET/CT hybrid acquisition systems, CT-derived attenuation maps enable a more accurate PET reconstruction. However, CT provides only very limited soft-tissue contrast and exposes the patient to an additional radiation dose. In comparison, Magnetic Resonance Imaging (MRI) provides good soft-tissue contrast and the ability to study functional activation and tissue microstructures, but does not directly provide patient-specific electron density maps for PET reconstruction.

The aim of the proposed work is to improve PET/MR reconstruction by generating synthetic CTs and attenuation-maps. The synthetic images are generated through a multi-atlas information propagation scheme, locally matching the MRI-derived patient's morphology to a database of pre-acquired MRI/CT pairs. Results show improvements in CT synthesis and PET reconstruction accuracy when compared to a segmentation method using an Ultrashort-Echo-Time MRI sequence.

1 Introduction

Positron Emission Tomography/Magnetic Resonance Imaging (PET/MRI) scanners are expected to offer a new range of applications in neuro-oncology, neurodegenerative diseases, such as Alzheimer's disease, and epilepsy [1]. To accurately quantify the radionuclide uptake, PET data need to be corrected for photon attenuation. The attenuation information is usually obtained from a transmission scan in standalone PET or derived from a Computed Tomography (CT) image in combined PET/CT. As MRI intensities do not reflect the electron densities, alternative methods must be developed for PET/MRI acquisitions. These methods can be classified in three categories: segmentation, atlas, and emission-based approaches. In segmentation-based methods, uniform linear attenuation coefficients are assigned to tissue classes obtained by segmenting an MRI image.

K. Mori et al. (Eds.): MICCAI 2013, Part I, LNCS 8149, pp. 147–154, 2013.

In atlas-based methods, an anatomical model or dataset is deformed to match the patient's anatomy in order to apply the attenuation map from the model to the patient data. The third class of methods exploits PET emission data from a time-of-flight PET system and anatomical information from MR images to compute the attenuation maps.

In the method from Martinez-Möller *et al.* [2], the body is segmented into four classes: background, lungs, fat and soft-tissues. While the results obtained in whole-body studies are satisfactory, the lack of bone information has a significant impact on the quantification of the radionuclide uptake in brain studies [3]. Keereman *et al.* [4] used Ultrashort-Echo-Time (UTE) sequences to distinguish cortical bone, air and soft tissue. Berker *et al.* [5] developed a 4-class tissue segmentation technique applied to brain studies. Cortical bone, air, fat and soft-tissues are segmented using a combined UTE/Dixon MRI sequence. Although the overall voxel classification accuracy reached is superior to the accuracy obtained without Dixon or UTE components, the bone segmentation is still inaccurate in complex regions such as nasal sinuses [5]. Johansson *et al.* [6] described a Gaussian mixture regression model that links the MRI intensity values to the CT Hounsfield units (HU). Schreibmann *et al.* [7] developed a multimodality optical flow deformable model that maps patient MRI images to a CT atlas. In the Hofmann *et al.* method [8], local information derived from a pattern recognition technique and global information obtained by an atlas registration are combined to predict a pseudo-CT image from a given MR image. All these methods assume a one-to-one correspondence between MRI and CT intensities. However, several materials such as cerebrospinal fluid, air and bone have similar intensities in a T1-weighted MRI image but distinct values in a CT image. Considering local information may enhance the results, but inaccuracies still remain at boundaries such as air and bone in the nasal sinuses.

The proposed method follows the principle of multi-atlas information propagation in order to synthesize an attenuation correction map from an MRI image. As an alternative to a one-to-one mapping from the observed MRI intensities to CT-like intensities, one can exploit the concept of morphological similarity between subjects. When used in the context of segmentation propagation [9], a set of segmented anatomical atlases from several subjects are mapped to a target subject and subsequently fused according to the morphological similarity between the mapped and the target anatomical images. This morphological similarity, normally interpreted as an image similarity measure, is used to enforce the fact that the most morphologically similar atlases should carry more weight during the fusion process [10]. This work will exploit the same idea in the context of intensity propagation and fusion. The developed algorithm makes use of a pre-acquired set of aligned MRI/CT image pairs from multiple subjects to propagate in a voxel wise fashion the CT intensities corresponding to similar MRIs. The proposed approach relies on the concept of morphological similarity rather than the assumption of one-to-one intensity mapping between the MRI and the CT. This enables the synthesization of a patient-specific pseudo CT image, from which the attenuation map is then generated.

2 Method

In PET/CT imaging, the main technique to correct for attenuation is to derive the attenuation coefficients from a CT image. In the case of a hybrid PET/MR scanner, the only anatomical and structural information available is an MR image. A diagram illustrating the proposed method in which a synthetic CT is obtained from a given MRI is shown in Figure 1.

2.1 MR-CT Database Preprocessing and Inter-subject Mapping

The database consists of pairs of T1-weighted MRI and CT brain images. For each subject, the MRI is affinely aligned to the CT using a symmetric approach based on Ourselin *et al.* [11]. Even though this is an intra-subject alignment, a full affine registration is used to compensate for possible gradient distortions in the MRI scans.

In order to synthesise the CT for a given MRI, one first needs to register all the MRIs in the atlas database to the target MRI. This inter-subject coordinate mapping is obtained using a symmetric global registration followed by a cubic B-spline parametrisation non-rigid registration, using normalised mutual information as a measure of similarity [12]. All the CTs in the atlas database are then mapped to the target subject using the transformation that maps the subject's corresponding MRI in the atlas database to the target MRI. Through this registration and resampling procedure, one obtains a series of MRI/CT pairs aligned to the MRI of the target subject.

2.2 CT Synthesis

The proposed framework uses a local image similarity measure between the target MRI and the set of registered MRIs as a metric of the underlying

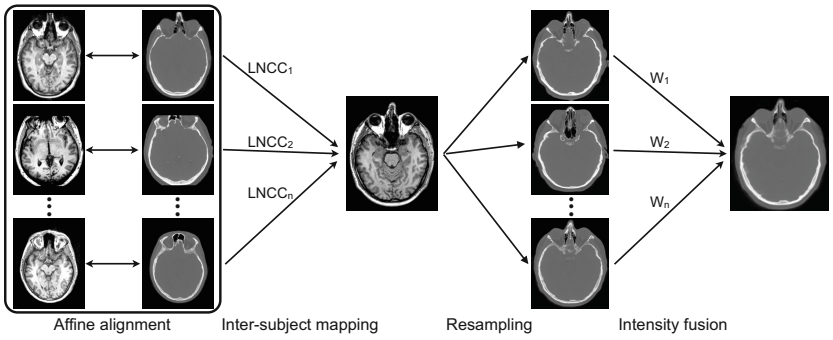

Fig. 1. CT synthesis diagram for a given MRI image. All the MRIs in the atlas set are registered to the target MRI. The CTs in the atlas set are then mapped using the same transformation to the target MRI. A similarity measure (LNCC) between the mapped and target MRIs is converted to weights (W) to reconstruct the target CT.

morphological similarity. Provided the local image similarity is a good approximation of the local morphological similarity between subjects, we assume that if two MRIs are similar at a certain spatial location, the two CTs will also be similar.

Image/Morphological Similarity. The morphological similarity between the target MRI and the registered MRIs from the atlas database is calculated locally using the normalised cross-correlation (LNCC) scheme proposed by Yushkevich *et al.* [13]. The LNCC similarity measure monitors the local quality of match between the MRI of the target subject and each of the warped MRIs from the atlas database. In this work, a convolution-based fast local normalised correlation coefficient proposed by Cachier *et al.* [14] is used. Let the target subject's MRI be denoted by I^{MRI} and its corresponding unknown CT be denoted by I^{CT}. For each of the N atlases in the database, let the mapped MRI and CT images of atlas n be denoted by J_n^{MRI} and J_n^{CT} respectively. The LNCC between I^{MRI} and J_n^{MRI} at voxel $\boldsymbol{v}$ is then given by:

$$\text{LNCC}_{\boldsymbol{v}} = \frac{\langle I^{MRI}, J_n^{MRI} \rangle_{\boldsymbol{v}}}{\sigma_{\boldsymbol{v}}(I^{MRI})\sigma_{\boldsymbol{v}}(J_n^{MRI})} \ . \tag{1}$$

As in [14], the means and standard deviations (std) at voxel $\boldsymbol{v}$ are calculated using a Gaussian kernel G, with a kernel std equal to 5 voxels, using convolution:

$$\overline{I}_{\boldsymbol{v}} = G * I(\boldsymbol{v}) \qquad \sigma(I)_{\boldsymbol{v}} = \sqrt{\overline{I^2}_{\boldsymbol{v}} - \overline{I}_{\boldsymbol{v}}^2} \qquad \langle I, J \rangle_{\boldsymbol{v}} = \overline{I \cdot J}_{\boldsymbol{v}} - \overline{I}_{\boldsymbol{v}} \cdot \overline{J}_{\boldsymbol{v}} \ ,$$

where $*$ denotes the convolution operator. High LNCC values indicate a better local match between the two MRI images.

As suggested by Yushkevich *et al.* [13], the range of LNCC can vary quite dramatically between subjects and locations. Thus, a ranking scheme similar to [13] is used. The LNCC at each voxel is ranked across all atlas images, with the rank being denoted by $R_{n\boldsymbol{v}}$. The ranks $R_{n\boldsymbol{v}}$ are then converted to weights by applying an exponential decay function:

$$W_{n\boldsymbol{v}} = \begin{cases} e^{-\beta R_{n\boldsymbol{v}}} & R_{n\boldsymbol{v}} < \kappa, \\ 0 & \text{otherwise} \ . \end{cases} \tag{2}$$

with $W_{n\boldsymbol{v}}$ being the weight associated with the n^{th} subject image at voxel $\boldsymbol{v}$ and κ being a truncation parameter. The weight function is restricted to the highest κ LNCCs, removing the influence of morphologically dissimilar subjects or mis-registration. Here, $N = 27$, κ is set to 9 and β to 0.5. Future work will involve an explicit optimisation of these values.

Intensity Fusion. Similarly to the label fusion framework suggested by Cardoso *et al.* [15], an estimate of the target subject's CT can be obtained by a spatially varying weighted averaging. The weights $W_{n\boldsymbol{v}}$ are used to reconstruct the target CT image I^{CT} at voxel $\boldsymbol{v}$ as follows:

$$I_{\boldsymbol{v}}^{CT} = \frac{\sum_{n=1}^{N} W_{n\boldsymbol{v}} \cdot J_{n\boldsymbol{v}}^{CT}}{\sum_{n=1}^{N} W_n} \ . \tag{3}$$

2.3 Attenuation Map

To obtain the attenuation map (μ-map), the synthetic CT image is resampled to the PET resolution. The resampled CT image is then matched to the PET's point spread function (PSF) by filtering it with a 6mm full-width at half-maximum Gaussian filter. According to [16], the CT values expressed in HU are converted to PET attenuation coefficients in cm^{-1} by a bilinear transformation:

$$\mu = \begin{cases} \mu_{\text{water}} \left(1 + \frac{I^{CT}}{1000}\right) & I^{CT} \leq 0 \text{ HU} \\ \mu_{\text{water}} \left(1 + \frac{I^{CT}}{1000} \frac{\rho_{\text{water}}(\mu_{\text{bone}} - \mu_{\text{water}})}{\mu_{\text{water}}(\rho_{\text{bone}} - \rho_{\text{water}})}\right) & I^{CT} > 0 \text{ HU} \end{cases} \tag{4}$$

where μ_{water} and μ_{bone} represent the attenuation coefficients at the PET 511 keV energy for water and bone respectively and ρ_{water} and ρ_{bone} represent the attenuation coefficients at the CT energy respectively. These values are set to $\mu_{\text{water}} = 0.096\,\mathrm{cm}^{-1}$, $\mu_{\text{bone}} = 0.172\,\mathrm{cm}^{-1}$, $\rho_{\text{water}} = 0.184\,\mathrm{cm}^{-1}$ and $\rho_{\text{bone}} = 0.428\,\mathrm{cm}^{-1}$

3 Validation and Results

Data. All the data used in this work were acquired with two scanners. The T1-weighted MRIs (3.0T; TR/TE, 1800ms/2.73ms; flip angle 9°; resolution $0.527 \times 0.527 \times 0.9$ mm^3) and UTE attenuation maps (resolution $1.562 \times 1.562 \times 1.562$ mm^3) were acquired on a Siemens Biograph mMR hybrid PET/MR scanner; the CTs (resolution $0.586 \times 0.586 \times 1.25$ mm^3), and reconstructed PETs (radiopharmaceutical: FDG; resolution $1.953 \times 1.953 \times 3.27$ mm^3) on a GE Discovery ST PET/CT scanner.

Validation Scheme. The synthesization performance of the proposed algorithm is validated against ground truth data. The quantitative validation consists of three steps:

- The pseudo CT (pCT) is compared to the subject's ground truth CT image at the original resolution, validating the accuracy of the CT reconstruction.
- The pCT is resampled to the PET's resolution and convolved with the point spread function, validating how accurate the CT synthesis is at the resolution relevant for PET reconstruction.
- The PET image is reconstructed using the pCT-derived μ-map and compared with the ground truth PET reconstructed using the CT-based μ-map, validating the accuracy of the PET attenuation correction.

The dataset consists of T1-weighted MRI, CT and PET brain images from 28 subjects. In 17 cases, MRI data are truncated at the front and back of the head. As UTE μ-map images are also available for 4 subjects, synthesization performance of the proposed algorithm is compared to the UTE-based synthesization method. All quantitative assessments are performed using a leave-one-out cross-validation scheme.

Table 1. Average (std) of the MAR between the ground truth (high-resolution CT, PET-resolution CT and CT-reconstructed PET) and the corresponding synthetic images, using both the proposed method (pCT) and UTE. The common datasets consist of 4 subjects with a non-truncated T1 and a known UTE μ-map, the untruncated datasets consist of 7 subjects with a non-truncated T1 but no associated UTE μ-map and the truncated datasets gather 17 subjects with a truncated T1 image. "No AC" corresponds to the residuals without attenuation correction. PETs are quantitatively normalised using the pons as the reference region.

	High-res CT		PET-res CT		Reconstructed PET		
	pCT	UTE	pCT	UTE	No AC	pCT	UTE
Common data (N=4)	100 (3)	190 (25)	77 (4)	194 (17)	1.66 (0.15)	0.23 (0.05)	0.74 (0.09)
Untruncated data (N=7)	102 (10)	-	73 (15)	-	0.85 (0.64)	0.12 (0.09)	-
Truncated data (N=17)	108 (10)	-	84 (10)	-	1.10 (0.51)	0.18 (0.10)	-

Pseudo CT Reconstruction Accuracy. Using only the MRI image of the subject, a pseudo CT image is generated using the proposed method. This generated CT is then compared to the ground truth CT. The metric used for validation is the mean absolute residual, defined as $\text{MAR} = \sum_{\boldsymbol{v}} |GT^{CT}_{\boldsymbol{v}} - I^{CT}_{\boldsymbol{v}}|$. This metric is estimated between the ground truth CT (GT^{CT}) and the pseudo CT (I^{CT}) for every subject in the database. The same MAR metric is also used to assess the synthesis accuracy after resampling the pCT to the PET resolution and simulating the PET PSF. When available, the MAR is computed between the UTE μ-map and the ground truth CT at both CT and PET resolutions. The average (std) MAR, measured in Hounsfield units, across all the subjects in the database and for both experiments is presented in Table 1. The error obtained with the pCT method is half that of the error obtained with the UTE method. The results also emphasize the robustness of the algorithm in the case of a truncated target MRI. Examples of ground truth CTs and μ-maps, pseudo CTs and pseudo μ-maps and UTE-based μ-maps are presented in Figure 2.

PET Reconstruction Accuracy. Due to the unavailability of the raw PET data, we make use of the PET reconstruction provided by the PET/CT scan-

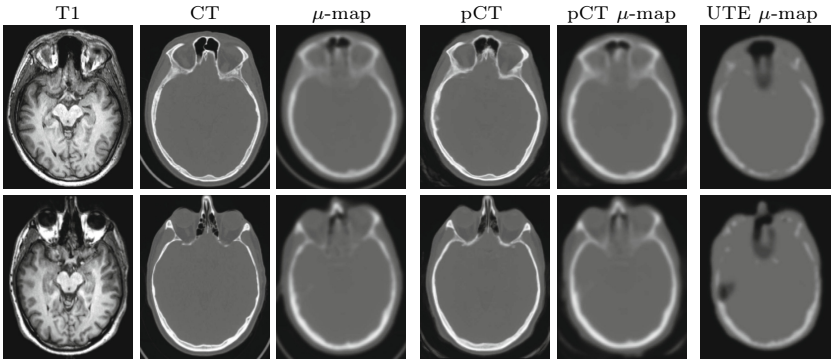

Fig. 2. Acquired T1-weighted MRI, CT and μ-map, pseudo CT and μ-map generated by the proposed method and UTE-based μ-map for two subjects

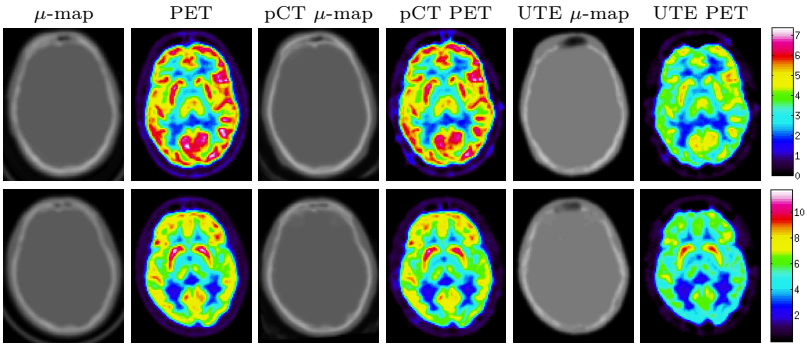

Fig. 3. (From left to right) The ground truth μ-map and PET reconstruction followed by the equivalent images generated using the proposed method and UTE-based methods, for two subjects. All methods are normalised to the same scale.

ner. To reconstruct the PET with the pCT-based μ-map, we follow a projection/reconstruction technique similar to Hofmann *et al.* [8]. The original PET, the original μ-map and the pCT-based μ-map are projected to obtain sinograms. The original attenuation correction is removed from the PET and the non-corrected PET is then corrected using the pCT μ-map. Following the same pipeline, we also reconstruct PET images using the CT μ-map (this PET is considered as the ground truth) and the UTE μ-map. The iterative reconstruction is performed using a GPU accelerated rotation-based projection and backprojection algorithm developed by Pedemonte *et al.* [17]. Results of PET reconstructions using different attenuation maps are displayed in Figure 3. The MAR is computed between the ground truth PET and the non-corrected, pCT and UTE-PET. Results are shown in Table 1. The error obtained using the pCT μ-map is three times smaller than the error obtained using the UTE μ-map.

4 Conclusion

This paper presents a simple CT and attenuation map synthesis algorithm based on a multi-atlas information propagation scheme. While the sharpness of the synthetic CT images is lower than the ground-truth subject's CT at the original resolution, this problem is greatly reduced at the resolution and PSF of the PET image. Overall, the proposed algorithm provides an improvement in PET reconstruction accuracy when compared to the UTE-based correction.

Acknowledgements. This work was supported by an IMPACT studentship funded jointly by Siemens and the UCL FES, the EPSRC (EP/K005278/1 and EP/H046410/1) and the CBRC Strategic Investment Award (#168).

References

1. Von Schulthess, G.K., Kuhn, F.P., Kaufmann, P., Veit-Haibach, P.: Clinical positron emission tomography/magnetic resonance imaging applications. Seminars in Nuclear Medicine 43(1), 3–10 (2013)

2. Martinez-Möller, A., Souvatzoglou, M., Delso, G., Bundschuh, R.A., Chefd'hotel, C., Ziegler, S.I., Navab, N., Schwaiger, M., Nekolla, S.G.: Tissue classification as a potential approach for attenuation correction in whole-body PET/MRI: evaluation with PET/CT data. Journal of Nuclear Medicine 50(4), 520–526 (2009)
3. Schleyer, P.J., Schaeffter, T., Marsden, P.K.: The effect of inaccurate bone attenuation coefficient and segmentation on reconstructed PET images. Nuclear Medicine Communications 31(8), 708–716 (2010)
4. Keereman, V., Fierens, Y., Broux, T., De Deene, Y., Lonneux, M., Vandenberghe, S.: MRI-based attenuation correction for PET/MRI using ultrashort echo time sequences. Journal of Nuclear Medicine 51(5), 812–818 (2010)
5. Berker, Y., Franke, J., Salomon, A., Palmowski, M., Donker, H.C.W., Temur, Y., Izquierdo-Garcia, D., Fayad, Z.A., Kiessling, F., Schulz, V.: MRI-based attenuation correction for hybrid PET/MRI systems: a 4-class tissue segmentation technique using a combined ultrashort-echo-time/Dixon MRI sequence. JNM 53(5) (2012)
6. Johansson, A., Karlsson, M., Nyholm, T.: CT substitute derived from MRI sequences with ultrashort echo time. Medical Physics 38(5), 2708 (2011)
7. Schreibmann, E., Nye, J.A., Schuster, D.M., Martin, D.R., Votaw, J., Fox, T.: MR-based attenuation correction for hybrid PET-MR brain imaging systems using deformable image registration. Medical Physics 37(5), 2101 (2010)
8. Hofmann, M., Steinke, F., Scheel, V., Charpiat, G., Farquhar, J., Aschoff, P., Brady, M., Schölkopf, B., Pichler, B.J.: MRI-based attenuation correction for PET/MRI: a novel approach combining pattern recognition and atlas registration. Journal of Nuclear Medicine 49(11), 1875–1883 (2008)
9. Heckemann, R.A., Hajnal, J.V., Aljabar, P., Rueckert, D., Hammers, A.: Automatic anatomical brain MRI segmentation combining label propagation and decision fusion. NeuroImage 33(1), 115–126 (2006)
10. Sabuncu, M.R., Van Leemput, K., Fischl, B., Golland, P.: A generative model for image segmentation based on label fusion. TMI 29(10) (2010)
11. Ourselin, S., Roche, A., Subsol, G.: Reconstructing a 3D structure from serial histological sections. Image and Vision Computing 19(2001), 25–31 (2000)
12. Modat, M., Ridgway, G.R., Taylor, Z.A., Lehmann, M., Barnes, J., Hawkes, D.J., Fox, N.C., Ourselin, S.: Fast free-form deformation using graphics processing units. Computer Methods and Programs in Biomedicine 98(3), 278–284 (2010)
13. Yushkevich, P.A., Wang, H., Pluta, J., Das, S.R., Craige, C., Avants, B.B., Weiner, M.W., Mueller, S.: Nearly automatic segmentation of hippocampal subfields in in vivo focal T2-weighted MRI. NeuroImage 53(4), 1208–1224 (2010)
14. Cachier, P., Bardinet, E., Dormont, D., Pennec, X., Ayache, N.: Iconic feature based nonrigid registration: the PASHA algorithm. CVIU 89(2-3) (2003)
15. Cardoso, M.J., Wolz, R., Modat, M., Fox, N.C., Rueckert, D., Ourselin, S.: Geodesic Information Flows. In: Ayache, N., Delingette, H., Golland, P., Mori, K. (eds.) MICCAI 2012, Part II. LNCS, vol. 7511, pp. 262–270. Springer, Heidelberg (2012)
16. Burger, C., Goerres, G., Schoenes, S., Buck, A., Lonn, A.H.R., Von Schulthess, G.K.: PET attenuation coefficients from CT images: experimental evaluation of the transformation of CT into PET 511-keV attenuation coefficients. European Journal of Nuclear Medicine and Molecular Imaging 29(7), 922–927 (2002)
17. Pedemonte, S., Bousse, A., Erlandsson, K., Modat, M., Arridge, S., Hutton, B.F., Ourselin, S.: GPU accelerated rotation-based emission tomography reconstruction. In: IEEE Nuclear Science Symposuim, pp. 2657–2661 (2010)